

Follow-up of 27 radio-quiet gamma-ray pulsars at 110–190 MHz using the international LOFAR station FR606

J.-M. Grießmeier^{1,2}, D. A. Smith^{3,4}, G. Theureau^{1,2,5}, T. J. Johnson^{6,7}, M. Kerr⁸, L. Bondonneau^{1,9},
I. Cognard^{1,2}, and M. Serylak^{10,11}

¹ LPC2E – Université d’Orléans/CNRS, France

e-mail: jean-mathias.griessmeier@cnrs-orleans.fr

² Station de Radioastronomie de Nançay, Observatoire de Paris – CNRS/INSU, USR 704 – Univ. Orléans, OSUC, Route de Souesmes, 18330 Nançay, France

³ Centre d’Études Nucléaires de Bordeaux Gradignan, IN2P3/CNRS, Université Bordeaux, 33175 Gradignan, France

⁴ Laboratoire d’Astrophysique de Bordeaux, Université Bordeaux, B18N, Allée Geoffroy Saint-Hilaire, 33615 Pessac, France

⁵ Laboratoire Univers et Théories LUTH, Observatoire de Paris, CNRS/INSU, Université Paris Diderot, 5 Place Jules Janssen, 92190 Meudon, France

⁶ College of Science, George Mason University, Fairfax, VA 22030, USA

⁷ Resident at Naval Research Laboratory, Washington, DC 20375, USA

⁸ Space Science Division, Naval Research Laboratory, Washington, DC 20375-5352, USA

⁹ LESIA, Observatoire de Paris, CNRS, PSL, SU/UP/VO, 92195 Meudon, France

¹⁰ South African Radio Astronomy Observatory, 2 Fir Street, Black River Park, Observatory 7925, South Africa

¹¹ Department of Physics and Astronomy, University of the Western Cape, Bellville, Cape Town 7535, South Africa

Received 19 March 2021 / Accepted 14 July 2021

ABSTRACT

Context. The *Fermi* Large Area Telescope has detected over 260 gamma-ray pulsars. About one quarter of these are labeled as radio-quiet, that is they either have radio flux densities $<30\ \mu\text{Jy}$ at 1400 MHz, or they are not detected at all in the radio domain. In the population of nonrecycled gamma-ray pulsars, the fraction of radio-quiet pulsars is higher, about one half.

Aims. Most radio observations of gamma-ray pulsars have been performed at frequencies between 300 MHz and 2 GHz. However, pulsar radio fluxes increase rapidly with decreasing frequency, and their radio beams often broaden at low frequencies. As a consequence, some of these pulsars might be detectable at low radio frequencies even when no radio flux is detected above 300 MHz. Our aim is to test this hypothesis with low-frequency radio observations.

Methods. We have observed 27 *Fermi*-discovered gamma-ray pulsars with the international LOw Frequency ARray (LOFAR) station FR606 in single-station mode. We used the LOFAR high band antenna band (110–190 MHz), with an average observing time of 13 h per target. Part of the data had to be discarded due to radio frequency interference. On average, we kept 9 h of observation per target after the removal of affected datasets, resulting in a sensitivity for pulse-averaged flux on the order of 1–10 mJy.

Results. We do not detect radio pulsations from any of the 27 sources, and we establish stringent upper limits on their low-frequency radio fluxes. These nondetections are compatible with the upper limits derived from radio observations at other frequencies. We also determine the pulsars’ geometry from the gamma-ray profiles to see for which pulsars the low-frequency radio beam is expected to cross Earth.

Conclusions. This set of observations provides the most constraining upper limits on the flux density at 150 MHz for 27 radio-quiet gamma-ray pulsars. In spite of the beam-widening expected at low radio frequencies, most of our nondetections can be explained by an unfavorable viewing geometry; for the remaining observations, especially those of pulsars detected at higher frequencies, the nondetection is compatible with insufficient sensitivity.

Key words. pulsars: general – telescopes – ISM: general

1. Introduction

The Large Area Telescope (LAT) on the *Fermi* satellite has strongly increased the number of known gamma-ray pulsars (see e.g., the “*Fermi* 2nd Pulsar Catalog” [Abdo et al. 2013](#), hereafter 2PC). A major update, “3PC”, which is in preparation, will characterize at least 260 gamma-ray pulsars¹. For the *Fermi* LAT pulsar detections, three different approaches have been

used ([Pletsch et al. 2012a](#)): (1) For some pulsars known from radio observations, gamma-ray pulsations have been detected using radio ephemerides, see for example [Smith et al. \(2019\)](#). (2) Radio searches of unassociated gamma-ray sources have revealed new radio pulsars, mostly millisecond pulsars (MSPs). A radio ephemeris could be then derived, allowing for the detection of gamma-ray pulsations. (3) Data from other unassociated gamma-ray sources have been searched for a large number of trial parameters (e.g., period, period derivative, position, among others), allowing for the detection of new “blind search” gamma-ray pulsars. In a half-dozen cases, radio follow-up and folding at the gamma-ray derived period identified these sources

¹ A list is maintained at <https://confluence.slac.stanford.edu/display/GLAMCOG/Public+List+of+LAT+Detected+Gamma-Ray+pulsars>

as radio pulsars (Clark et al. 2018). Some of these are very faint: In 2PC, a pulsar is designated as radio-quiet (RQ) if its flux density at 1400 MHz, S_{1400} , is $<30 \mu\text{Jy}$, for which J1907+0602 with $S_{1400} = 3.4 \mu\text{Jy}$ is an example (Abdo et al. 2010). In the majority of cases, however, no radio counterpart has been detected. Approximately half of the 142 nonrecycled gamma-ray pulsars are radio-loud ($S_{1400} \geq 30 \mu\text{Jy}$), the rest are radio-quiet (Wu et al. 2018).

If detected, radio emission from a gamma-ray pulsar provides extra information, such as the pulsar’s dispersion measure (DM). Combined with a geometrical model of the Galaxy (e.g., Cordes & Lazio 2002; Yao et al. 2017), this provides an approximate source distance. This has motivated a number of radio follow-up studies for known gamma-ray pulsars².

Most of these follow-up studies have been performed between 820 and 1500 MHz. Studies at lower frequencies are interesting for two reasons. First, the spectra of most pulsars are usually well described by a power law, but different pulsars have different spectral indices (Sieber 1973; Maron et al. 2000; Jankowski et al. 2018). Some of the gamma-ray pulsars might have a steeper than average spectrum with a very low (possibly undetected) flux density at high frequencies, but a high (and potentially detectable) flux at lower frequencies. Second, the radio beams of many pulsars are wider at low frequencies (e.g., Sieber et al. 1975), such that a beam that narrowly misses Earth at higher frequencies could still intersect Earth at lower frequencies. Such beam widening is expected, for example, from the radius-to-frequency mapping model (i.e., higher frequency emission originating closer to the neutron star than lower frequency emission, Cordes 1978).

With beam widening in mind, Maan & Aswathappa (2014) performed follow-up observations of *Fermi* LAT detected pulsars at 34 MHz using the Gauribidanur telescope. However, many pulsars show a spectral break or turnover between 50 and 100 MHz (e.g., Sieber 1973; Kuzmin et al. 1978; Izvekova et al. 1981), so that observations at 34 MHz may miss pulsars which might be detectable at frequencies above this spectral turnover. In addition, scatter broadening may lead to a pulse width exceeding the pulse period, making detection difficult. Scatter broadening is usually assumed to scale as $\propto f^{-4}$, where f is the observing frequency, so that low-frequency observations are particularly strongly impacted. Indeed, Maan & Aswathappa (2014) did not detect any periodic signal above their detection threshold (8σ) at 34 MHz, but they were able to determine flux density upper limits.

Flux density upper limits at 150 MHz were derived for all observable radio-quiet gamma-ray pulsars using the GMRT all-sky survey TGSS (Frail et al. 2016). However, the integration time per pointing was only 15 min, leading to relatively weak constraints on the flux density.

For these reasons, we systematically followed up on all 27 northern sky nonrecycled radio-quiet gamma-ray pulsars with targeted observations and searched for radio pulsations at low frequencies. For this, we used the international LOw Frequency ARray (LOFAR) station FR606 in Nançay in stand-alone mode, observing in the high band antenna (HBA) frequency range (110–190 MHz).

This paper is organized as follows: Section 2 discusses the interest of low-frequency observations (higher flux at low frequencies in Sect. 2.1 and beam widening at low frequencies in

Sect. 2.2). Section 3 describes the methods used: We describe how the targets were selected (Sect. 3.1), how the observations were performed (Sect. 3.2), how the data were processed (Sect. 3.3), and how flux density upper limits were calculated (Sect. 3.4). In Sect. 4, we present the results of our observations. In Sect. 5, we discuss the pulsars’ geometry: We first discuss the consequences of beam widening for a uniform distribution of pulsar geometries (Sect. 5.1), then explain how we determined the pulsars’ geometry from the observed gamma-ray profiles (Sect. 5.2), and finally discuss the consequences of beam widening for those specific geometries (Sect. 5.3). Section 6 closes with some concluding remarks.

2. Radio beam basics

2.1. Radio spectra

At frequencies ≥ 200 MHz, the spectra of most pulsars are well described by a single spectral index (Sieber 1973; Maron et al. 2000; Jankowski et al. 2018). However, different pulsars have different spectral indices, with a wide spread. Throughout this work, we adopt an average spectral index of -1.6 with a standard deviation of 0.54 (Jankowski et al. 2018). We assume that the spread of spectral indices is at least partially physical; for this reason, we use their standard deviation rather than their standard error. This range of values formally encompasses those given by other works, such as Maron et al. (2000) and Lorimer et al. (1995). At frequencies below 200 MHz, the spectral index flattens and most nonrecycled pulsars show a turnover between 50 and 100 MHz (e.g., Sieber 1973; Kuzmin et al. 1978; Izvekova et al. 1981; Bilous et al. 2016, 2020; Jankowski et al. 2018; Bondonneau et al. 2020). This is not accounted for in our calculations, and the extrapolated flux density limits at frequencies <200 MHz are probably slightly overestimated.

With a spectral index of -1.6 ± 0.54 , we can expect flux densities to be higher at 150 MHz than at 1400 MHz by 1–2 orders of magnitude. This gain is partially offset by the increased sky temperature against which the pulsar has to be detected; even so, for a comparable telescope gain, or effective area, we can expect to detect fainter pulsars. This is particularly true for those that have a steeper than average spectral index.

No matter how steep the spectrum may be, a pulsar that is intrinsically faint or too distant remains undetectable. A consensus about pulsar radio luminosity L_r does not exist, but it is frequently assumed that it depends on the rotation period (P) and period derivative (\dot{P}) as $L_r = L_0 P^a \dot{P}^b$, albeit with large uncertainties on the parameters a and b and with a large spread, that is to say $P^a \dot{P}^b$ and L_r are poorly correlated. As an example, Johnston & Karastergiou (2017) found a, b such that $L_r = \dot{E}^{1/4}$ where \dot{E} is the spindown power. Distance d affects detectability in two ways: First, $S_{1400} \propto L_r/d^2$. Second, a large d implies a large dispersion measure, especially at low Galactic latitudes. For pulsars with periods $\lesssim 500$ ms and observations at 150 MHz, we are limited to $\text{DM} \lesssim 500 \text{ pc cm}^{-3}$; for higher DM values, the expected scattering time exceeds the pulsar’s rotation period (see Sect. 3.3). Thus some pulsars are not seen even if the spectrum is steep and/or the beam broadens into the line of sight, as discussed below.

2.2. Beam widening

A simple radio beam model suffices for this work. Following Cordes (1978) or, equivalently, the Pulsar Handbook (Lorimer & Kramer 2005, Sect. 3.4), radio emission is centered

² For the studies mentioned in the following, measured flux density values or upper limits thereof are given in Appendix A for the pulsars that overlap with our selection.

around the neutron star magnetic dipole axis. The dipole is inclined with an angle α from the rotation axis, and the line of sight from Earth makes an angle ζ with the rotation axis. High-energy electrons follow the magnetic field lines and radiate at radio frequencies that depend on the field line curvature. Hence, radio emission is a cone-shaped beam of radius

$$\rho \approx \sqrt{\frac{9\pi r_{\text{em}}}{2cP}} = \frac{3}{2} \sqrt{\frac{r_{\text{em}}}{r_{\text{LC}}}}, \quad (1)$$

where r_{em} is the height of radio emission and $r_{\text{LC}} = cP/(2\pi)$ defines the “light cylinder”, the radius at which an object co-rotating with the neutron star with a spin period P would reach the speed of light, c . Typical values of $r_{\text{em}} = 300$ km and $P = 0.1$ s give $\rho \approx 20^\circ$. The radio beam sweeps Earth only if $(\alpha + \rho) > \zeta > (\alpha - \rho)$, making the pulsar potentially radio-loud (RL). Following Gil et al. (2002), the observed pulse has a width W given by

$$\sin^2\left(\frac{W}{4}\right) = \frac{\sin^2(\rho/2) - \sin^2(\beta/2)}{\sin \alpha \cdot \sin \zeta}, \quad (2)$$

where $\beta = (\zeta - \alpha)$ is the angle between the magnetic axis and the line of sight. For RQ pulsars, $|\beta| > \rho$ and W is undefined. If the beam grazes Earth, W may be so small that the radio flux integrated over the narrow pulse is below a given radio telescope’s sensitivity, and if detected it is likely very faint: We call these borderline cases radio-faint (RF).

From the Pulsar Handbook, $\rho = A_1 f^{-q} + A_0$ or $r_{\text{em}} = B_1 f^{-p} + B_0$, where f is the radio frequency. For positive values of the index p , Eq. (1) leads to beam widening at low radio frequencies. This is called radius-to-frequency mapping (RFM). The parameters (B_0, B_1, p) have different values for different pulsars. For example, Thorsett (1991) studied seven multi-component pulsars that have been observed over a wide frequency range, finding the outer components to be separated by angles of 5 – 10° at 1400 MHz, but up to 30° at 150 MHz. Similarly, Xilouris et al. (1996) studied eight pulsars. Their Fig. 2 shows the profile widths to approximately double between 1000 and 100 MHz.

While W increasing at low frequency f is common, this is not the case for all pulsars. Pilia et al. (2016) determined the index δ for 100 pulsars, such that the observed width at 10% of the pulse amplitude is $w_{10} \propto f^\delta$ (see their Figs. 3 and 7). For $\sim 20\%$ of the pulsars, they find $\delta > 0$, meaning that the pulse narrows with decreasing frequency. However, they did indeed obtain $\delta < 0$ for 80% of the pulsars and found an average value of $\langle \delta \rangle \sim -0.1$ (weighted mean over all values of δ). Thus, a significant fraction of their sample roughly agrees with the expectation from simple RFM.

Based on these observations, we assume RFM to hold. More specifically, we used the parameterization of Story et al. (2007, Eqs. (9) and (10)), which is based on the model of Kijak & Gil (1997, 1998, 2003). In terms of the above parameterization, this is equivalent to $B_0 = 0$ and $p = 0.26$. Using $P = 100$ ms and $\dot{P} = 1 \times 10^{-15} \text{ s s}^{-1}$, this model gives a beam width of 16.8° at 1400 MHz and 22.5° at 150 MHz. In Sect. 5.2, we combine these values with geometrical constraints (α, ζ) extracted from the gamma-ray profiles to predict radio detectability. The comparison of these model results to pulsed emission discovered with FR606 (or the upper limits thereof) provides useful data for emission models.

3. Methods

3.1. Target selection

To a good approximation, the effective area of the FR606 antenna array is

$$A_{\text{eff}} = A_{\text{eff}}^{\text{max}} \cos^2 z, \quad (3)$$

where z is the zenith angle of the source and $A_{\text{eff}}^{\text{max}} = 2048 \text{ m}^2$ (van Haarlem et al. 2013, Appendix B). For the telescope’s latitude ($\lambda = 47.35^\circ$), a declination limit of $\delta > -10^\circ$ ensures $\cos^2 z > 0.28$ at pulsar culmination, so that the telescope can be used with a meaningful sensitivity for a few hours on a given target each day. We thus selected the 20 radio-quiet pulsars in 2PC with $\delta > -10^\circ$, excluding Geminga (J0633+1746), which has already been extensively explored at low radio frequencies (Maan 2015, and references therein). In addition, we included seven pulsars discovered after 2PC (Pletsch et al. 2013; Clark et al. 2015, 2017; Wu et al. 2018). This leaves us with a total of 27 targets, which are listed in Table 1 (Col. 1).

All of our targets have already been observed by radio telescopes, with observing frequencies between 34 and 2000 MHz (see Table A.1 for the full list of observations). Table 1 (Cols. 6–8) shows the flux density upper limits for the most constraining of the previous observations. Detections rather than upper limits are denoted as such; in those cases, we indicate the equivalent flux density, assuming $W/P = 0.1$, rather than the measured flux density, with the measured value for the fractional pulse width W/P (see Appendix A). Column 9 gives the corresponding flux density limit at our observing frequency of 150 MHz for an assumed spectral index of -1.6 .

3.2. Observations

The observations were carried out on the International LOFAR Station in Nançay, FR606. LOFAR is fully described in Stappers et al. (2011) and van Haarlem et al. (2013). LOFAR stations have two different frequency bands: We used the HBA band (i.e., 110–190 MHz, with a center frequency of 149.9 and a total bandwidth of 78.125 MHz), for which the station consists of 96 antenna tiles, each of which is made up of 16 dual-polarization antenna elements. The signals from individual HBA tiles were coherently summed, creating a digital telescope.

While a single LOFAR station as used here only has a limited effective area or telescope gain, it allows for very flexible scheduling, especially for long observations. The capability of this setup for pulsar science has already been demonstrated (Rajwade et al. 2016; Mereghetti et al. 2016; Bondonneau et al. 2017, 2020; Michilli et al. 2018; Hermsen et al. 2018; Donner et al. 2019; Porayko et al. 2019; Tiburzi et al. 2019).

Long observing sessions were split into individual observations typically lasting one hour. Each target was observed between 7×1 h and 16×1 h, amounting to a total of 346 h of telescope time (on average approximately 13 h per target). To ensure phase coherence, the time span of our radio observations was at most 15 days for each pulsar. The analysis of test data showed that daytime observations contained intense radio frequency interference (RFI) and they did not provide data of a sufficiently good quality. To determine which fraction of the day allowed for high-quality observations, we observed a well-known pulsar (B0105+68, period $P \sim 1.07$ s, $\text{DM} \sim 61.06 \text{ pc cm}^{-3}$) with the same setup and pipeline as for sources of interest. Even though the pipeline includes RFI cleaning, the pulsar was not detected in daytime observations, while

Table 1. Northern radio-quiet gamma-ray pulsars.

Pulsar	l ($^{\circ}$)	b ($^{\circ}$)	P (ms)	$10^{-34} \dot{E}$ (erg s $^{-1}$)	f_{ref} (MHz)	S_{ref} (mJy)	Ref.	$S_{150}^{\text{extrapol}}$ (mJy)	N_{obs}	T_{sky} (K)	$t_{\text{obs}}^{\text{eff}}$ (h)	S_{150}^{min} (mJy)	s
J0002+6216*	117.33	-0.07	115.4	15.3	1400	0.022 (detection)	1,2,9	~0.78	9	859	6.5	<2.1	>-2.1
J0007+7303	119.66	10.46	315.9	44.8	820	<0.012	3	<0.18	9	619	5.4	<1.7	
J0106+4855*	125.47	-13.87	83.2	2.9	820	0.030 (detection)	4	~0.45	12	482	10.4	<1.3	>-2.2
J0357+3205	162.76	-16.01	444.1	0.6	327	<0.043	3	<0.15	12	374	8.9	<0.8	
J0359+5414	148.23	0.88	79.4	131.8	1400	<0.015	1,2	<0.53	12	716	10.5	<1.7	
J0554+3107	179.06	2.70	465.0	5.6	1400	<0.066	5	<2.4	11	483	7.6	<1.2	
J0622+3749	175.88	10.96	333.2	2.7	820	<0.032	4	<0.48	7	457	5.6	<1.4	
J0631+0646*	204.68	-1.24	111.0	10.4	1400	0.018 (detection)	1,2,9	~0.64	7	641	2.0	<3.2	>-2.3
J0633+0632	205.09	-0.93	297.4	11.9	1510	<0.003	3	<0.12	9	641	2.0	<2.3	
J1836+5925	88.88	25.00	173.3	1.1	820	<0.010	3	<0.15	3	493	2.1	<2.5	
J1838-0537	26.51	0.21	145.7	593.3	2000	<0.009	6	<0.57	4	4500	0.6	<26	
J1846+0919	40.69	5.34	225.6	3.4	1510	<0.004	8	<0.16	2	1370	0.9	<7.6	
J1906+0722	41.22	0.03	111.5	102.2	1400	<0.021	7	<0.75	9	2830	3.0	<8.0	
J1907+0602*	40.18	-0.89	106.6	282.4	1510	0.005 (detection)	10,3	~0.20	11	2510	3.2	<7.1	>-3.1
J1932+1916	54.66	0.08	208.2	40.7	1400	<0.075	5	<2.7	8	1410	4.1	<2.9	
J1954+2836	65.24	0.38	92.7	104.8	1510	<0.004	8	<0.16	11	1150	8.2	<2.1	
J1957+5033	84.60	11.00	374.8	0.5	820	<0.025	8	<0.38	10	613	8.6	<1.3	
J1958+2846	65.88	-0.35	290.4	34.2	1510	<0.005	3	<0.20	12	1150	8.3	<2.0	
J2017+3625	74.51	0.39	166.7	1.2	1510	<0.005	1,2	<0.20	13	554	8.1	<1.3	
J2021+4026	78.23	2.09	265.3	11.4	2000	<0.011	3	<0.69	13	2830	10.3	<3.2	
J2028+3332	73.36	-3.01	176.7	3.5	1510	<0.004	4	<0.16	7	921	5.2	<1.9	
J2030+4415	82.34	2.89	227.1	2.2	820	<0.019	4	<0.29	12	1420	10.1	<2.2	
J2032+4127*	80.22	1.03	143.2	36.3	2000	0.05 (detection)	11,3	~3.2	11	1600	9.6	<2.6	>-1.5
J2055+2539	70.69	-12.52	319.6	0.5	327	<0.085	8	<0.30	9	509	5.3	<1.3	
J2111+4606	88.31	-1.45	157.8	143.6	820	<0.033	4	<0.50	9	886	7.2	<1.9	
J2139+4716	92.63	-4.02	282.8	0.3	820	<0.034	4	<0.52	11	730	9.9	<1.1	
J2238+5903	106.56	0.48	162.7	88.8	820	<0.027	3	<0.41	11	1080	9.7	<1.9	

Notes. Column 1: name of the pulsar (pulsars with know radio emission are denoted with *). Columns 2 and 3: Galactic coordinates for each pulsar. Column 4: pulsar period (P). Column 5: spindown luminosity \dot{E} . Columns 6 and 7: observing frequency and measured mean flux density (or upper limit) for the most constraining observation (assuming a spectral index of -1.6). Column 8: Reference (for Cols. 6 and 7). Column 9: flux density (or upper limit) from Cols. 6 and 7 extrapolated to an observing frequency of 150 MHz (using a spectral index of -1.6). Column 10: the number of good observations (usually one hour) used in the final analysis (i.e., with a sufficiently low RFI level). Column 11: sky temperature. Column 12: the equivalent duration of the dataset under the assumption of nominal gain, as given by Eq. (5). Column 13: flux density upper limit at 150 MHz (in the band 110–190 MHz) as determined in this work. Column 14: limit on the spectral index s derived from the most constraining previous detection (Cols. 6 and 7) and our flux density limit (Col. 13).

References. (1) Clark et al. (2017), (2) Wu et al. (2018), (3) Ray et al. (2011), (4) Pletsch et al. (2012b), (5) Pletsch et al. (2013), (6) Pletsch et al. (2012a), (7) Clark et al. (2015), (8) Saz Parkinson et al. (2010), (9) J. Wu (priv. comm.), (10) Abdo et al. (2010), (11) Camilo et al. (2009).

it was clearly detected in all nighttime observations. For this reason, all observations of the sources of interest were taken at night.

Despite this precaution, a number of observations showed high RFI levels, and they had to be discarded subsequently (observations were discarded if RFI led to false candidates at apparent $S/N > 7$ even after RFI cleaning, see next section). In the end, only 255 h of observations with low RFI levels were retained (apparent $S/N < 7$), and the final analysis was based on between 2 and 13 h per target (Table 1, Col. 10 gives the number of observing sessions lasting typically 1 h; Col. 12, the equivalent duration of a zenith observations, $t_{\text{obs}}^{\text{eff}}$, is explained in Sect. 3.4).

3.3. Data analysis

For the data analysis, we used the standard pulsar tools *tempo2* (Hobbs et al. 2006), *DSPSR* (van Straten & Bailes 2011), *PSRCHIVE* (van Straten et al. 2012), and *COASTGUARD*³ (Lazarus et al. 2016). We folded the data at the period

determined by the LAT rotation ephemeris, thus leaving the pulsar’s dispersion measure (DM) as the only free parameter during the data analysis. In detail, we proceeded as described in the following.

Shortly before the observation, an ephemeris was constructed using *Fermi* LAT data. LAT radio-quiet pulsars are necessarily bright in gamma rays: Faint gamma-ray sources are too poorly localized and their photon arrival times are too infrequent to allow for effective blind pulsation searches. The gamma-ray brightness of our pulsar sample made it easy to extend their rotation ephemerides to cover the FR606 observation epochs using the method detailed in Kerr et al. (2015). We started with the ephemerides available from the references in Table 1 for each pulsar. These yield a constant gamma-ray phase to the end of the ephemeris validity, and well beyond for the more stable pulsars. From these, we made a template pulse profile using time intervals yielding profiles with a significance of 3σ (typically a week to a month, depending on the flux). Cross-correlating the profiles with the template determines a LAT time of arrival for each interval. With these times of arrival, *tempo2* (Hobbs et al. 2006) can then be used to improve the ephemeris. If the gamma-ray pulse is lost beyond the end of ephemeris validity period, it can generally be recovered after only a few iterations. We thus

³ https://github.com/plazar/coast_guard/

obtained an ephemeris for each of the 27 pulsars that is valid at the epoch of the FR606 observation.

During the observation, the full data stream was split on four different data acquisition machines (each receiving one quarter of the total bandwidth). The LuMP software⁴ was used to recorded the data.

After the observation, the four datasets (one per data acquisition machine) were each folded at the initial *Fermi* LAT period using DSPSR (van Straten & Bailes 2011) and channelized into 2440 channels of ~ 10 kHz. The number of channels was chosen as a compromise between the available computing resources and the expected loss of sensitivity due to DM smearing (the associated factor $\beta_{\delta\text{DM}}$ is quantified in Sect. 3.4). Subsequently, the borders of the bands were removed (low sensitivity of the antennas near the edge of their bandpass), so that in total 8000 useful frequency channels were kept (the frequency range of 110–190 MHz).

Then, the data were cleaned of RFI using COASTGUARD (Lazarus et al. 2016). Typically, $\sim 3\%$ of the data retained in the final step were flagged (with a maximum flagged fraction of 8.4%).

Subsequently, the data were rebinned to subintegrations of 300 s in order to reduce the data volume and speed up the post-processing. In the next step, the data from the four acquisition machines were combined.

A few months after the observation, an improved ephemeris based on *Fermi* LAT data was constructed (based on the extended *Fermi* LAT time series). The datasets (the 300 s subintegrations) were refolded with this improved ephemeris.

Using pdmp, we searched each individual observation session (~ 1 h) for a dispersed, periodic radio signal at the *Fermi* LAT period. This search was performed for all pulsars, including those already detected in radio: The DM precision of the high frequency observations might not be good enough (the effect of a small DM error is 100 times stronger at 150 MHz than at 1500 MHz); also, the precise DM value could have changed since the detection. We used 3980 trial DM values between 2 and 400 pc cm⁻³ in steps of 0.1 pc cm⁻³ (incoherent dedispersion). For 19 of our 27 lines of sight, the Galactic electron density model NE2001 (Cordes & Lazio 2002) predicts a maximum DM of less than 400 pc cm⁻³. For the eight remaining lines of sight (all close to the Galactic plane), the corresponding estimated scattering time at 150 MHz (assuming a scatter broadening spectral index of -4) already exceeds the pulsar's period, rendering an extension to even higher DM values useless. The result is similar for the YMW16 model (Yao et al. 2017): For 17 lines of sight, the maximum DM is below 400 pc cm⁻³, and for most of the remaining ten lines of sight, the estimated scattering time at 150 MHz exceeds the pulsar's period. The only exceptions are J1958+2846, J2021+4026, and J2030+4415, for which a maximum DM of ~ 500 would have been a slightly better choice.

Manual inspection showed that all observation sessions for which pdmp produced a high signal-to-noise ratio (S/N) were in fact corrupted by remaining RFI and showed high values for a wide range of DM values. For this reason, all observation sessions with a value of apparent $S/N \geq 7$ were discarded.

The remaining observation sessions of each target (between two and 13 sessions depending on the target) were added together using psradd.

For the combined files (one per target), we searched again for dispersed, periodic signals using pdmp. All candidate detections with a value of $S/N \geq 5$ (a total of 1657 candidates) were inspected manually.

This procedure was tested and validated on a well-known pulsar (B0105+68, period $P \sim 1.07$ s, DM ~ 61.06 pc cm⁻³). We then processed the observations of the 27 pulsars of Table 1 in this way; no pulsed radio signal was detected. To quantify our nondetections, we calculated the flux density upper limits, taking the elevation of the pulsar during each observing session into account (see following section).

3.4. Flux density upper limits

In none of our observations was a pulsar radio signal detected. Upper limits for the pulse-average flux were calculated following the Pulsar Handbook:

$$S_{\min} = \frac{S/N_{\min} (T_{\text{rec}} + T_{\text{sky}})}{\beta_{\delta\text{DM}} G_{\text{nom}} \sqrt{n_p t_{\text{obs}}^{\text{eff}} \Delta F_{\text{eff}}}} \sqrt{\frac{W}{P - W}}, \quad (4)$$

where a value of $S/N_{\min} = 5$ was assumed as a threshold in the S/N required for a detection, $T_{\text{rec}} = 422$ K is the receiver temperature (as derived from measurements by Wijnholds & van Cappellen 2011). The sky temperature T_{sky} depends on the sky position of the observed target; it is taken from the sky map at 408 MHz by Haslam et al. (1982) and was scaled to our frequencies using $f^{-2.55}$ (Lawson et al. 1987). The values for T_{sky} are given in Table 1 (Col. 11). Furthermore, $\beta_{\delta\text{DM}}$ is the loss of sensitivity due to imperfect DM gridding (see below), G_{nom} is the nominal telescope gain for a pointing near zenith, n_p is the number of polarizations (in all of our observations, $n_p = 2$), $t_{\text{obs}}^{\text{eff}}$ is the effective observing time for each pulsar (see below), and ΔF_{eff} is the effective frequency bandwidth of each observation after RFI cleaning. Finally, P is the pulsar period and W is the width of the pulse; for all pulsars, we assumed $W/P = 0.1$.

With our grid of trial DMs, the DM error δDM of the best trial is at most 0.05 pc cm⁻³. This leads to a slight loss in the S/N and thus in sensitivity. Using Cordes & McLaughlin (2003, Eqs. (12) and (13)), a center frequency of 149.9 MHz, a total bandwidth of 78.125 MHz, and $W/P = 0.1$, we find values in the range from $0.75 \leq \beta_{\delta\text{DM}} \leq 0.99$ for our sample, depending on the pulsar's period. These values were taken into account for the calculation of the flux density limits in Table 1.

For the nominal gain, we used $G_{\text{nom}} = A_{\text{eff}}^{\text{max}} / (2k_B) = 0.74$ K Jy⁻¹, which is equivalent to the effective area of $A_{\text{eff}}^{\text{max}} = 2048$ m² of the international LOFAR station FR606 for a pointing near zenith at an observing frequency of 150 MHz (van Haarlem et al. 2013, Appendix B). As the elevation of the pulsar varies during an observation, the projected area of the antenna array varies over time, cf. Eq. (3). Assuming the effective area is approximately constant over an observation of approximately one hour, the effective observing time after N_{obs} observations (with an effective area $A_{\text{eff},i}$ for the i th observation) is given by

$$t_{\text{obs}}^{\text{eff}} = \sum_{i=1}^{N_{\text{obs}}} t_i \left(\frac{A_{\text{eff},i}}{A_{\text{eff}}^{\text{max}}} \right)^2. \quad (5)$$

It is important to note that this implies that observations at a low elevation (and thus with $A_{\text{eff},i} \ll A_{\text{eff}}^{\text{max}}$) contribute only

⁴ <https://github.com/AHorneffer/lump-lofar-und-mpifr-pulsare>

marginally to the combined observation. The values of $t_{\text{obs}}^{\text{eff}}$ are given in Table 1 (Col. 12).

The values of $A_{\text{eff},i}$ and T_{sky} were calculated using the LOFAR calibration tool `lofar_fluxcal.py` (Kondratiev et al. 2015). The software makes use of the Hamaker beam model (Hamaker 2006, and references therein) and the `mscorpol`⁵ package to calculate the Jones matrices for a given frequency and sky coordinates.

With this, the upper limits on the flux density, S_{min} , were calculated, and the values are given in Table 1 (Col. 13). The implications are discussed in Sect. 4.

4. Results

No radio emission was detected for any of our targets. At our observing frequency of 150 MHz, we obtained flux density upper limits between 0.8 mJy and 26 mJy (the values are given in Col. 13 of Table 1). The large differences in the upper limits for different targets result from four effects: (a) The number of 1 h observations was different for different targets; (b) during some nights, the RFI conditions were worse than during others, forcing us to remove a larger number of observations from processing; (c) the low elevation of some sources led to a low effective observing time $t_{\text{obs}}^{\text{eff}}$ despite a large number of observations N_{obs} ; and (d) depending on the direction, the background sky temperature T_{sky} varied by more than one order of magnitude. In particular, we note that our flux density limits are less constraining for J1838–0537 (26 mJy), J1846+0919 (7.6 mJy), J1906+0722 (8.0 mJy), and J1907+0602 (7.1 mJy) than for our other targets. This is related to their proximity to the Galactic plane (Galactic coordinates are given in Table 1, Cols. 2 and 3), which causes a high sky temperature (T_{sky} , Table 1 Col. 11), and at the same time this reduces the effective area of the telescope because of their low declination (and thus leads to a small $t_{\text{obs}}^{\text{eff}}$, Col. 12). We obtained our most constraining flux density limit of 0.8 mJy for J0357+3205, where the sky temperature is particularly low (far off the Galactic plane) and for which RFI conditions were good, so that we have a large number of usable observations.

Table 1 shows the most constraining previous observation for each pulsar, assuming a spectral index of -1.6 . The observing frequency and the upper limit for the flux density are given in Cols. 6 and 7, and the equivalent flux density at 150 MHz is shown in Col. 9.

The same data are displayed in Fig. 1⁶, in which we compare our flux density upper limits (empty blue squares) to upper limits (empty red triangles) and detections (filled green circles, with a typical error bar of 30%) obtained by previous observation campaigns (all values are summarized in Table A.1). As can be seen in Fig. 1, our nondetections are compatible with the nondetection of those 21 of our targets that have been studied with imaging observations at 147.5 MHz using GMRT (Frail et al. 2016); our observations do, however, provide more stringent upper limits (by approximately one order of magnitude). The remaining six pulsars have never before been observed in this frequency range.

To test whether our upper limits are compatible with previous observations at different frequencies, we assume a spectral index of -1.6 ± 0.54 (see Sect. 2.1). To compare this to previous

nondetections, the dark blue lines in Fig. 1 represent flux density limits equivalent to our observation, assuming an average spectral index of -1.6 , and the shaded areas between the light blue lines correspond to a spectral index of -1.6 ± 0.54 (see Sect. 2.1). Figure 1 shows that our upper limits are compatible with all previous upper limits. For J0554+3107, our upper limit is more constraining than the previous observation by a factor ~ 2 .

Five of the pulsars we observed have been detected at higher radio frequencies, but they remain undetected in our observations. In Table 1, these pulsars are denoted with * in Col. 1, and limits for the spectral index s are given in Col. 14. For these pulsars, the dark green lines in Fig. 1 represent flux density limits equivalent to the most constraining detection, assuming an average spectral index of -1.6 , and the shaded areas between the light green lines correspond again to a spectral index of -1.6 ± 0.54 (see Sect. 2.1).

For J0002+6216, radio emission has been reported at frequencies of 1400 and 2000 MHz (Clark et al. 2017; Wu et al. 2018). When combined, these two observations hint at a spectral index shallower than average (-1.2). However, as both observing frequencies are not widely separated, the spectral index is not very well constrained. Our nondetection is compatible with both previous observations and constrains the spectral index to values > -2.1 .

The pulsar J0106+4855 has been detected at 820 MHz (Pletsch et al. 2012b). With our setup, a nondetection is expected as long as the spectral index is > -2.2 .

J0631+0636 has been detected at 327, 1400, and 1510 MHz. The two available flux measurements hint at a spectral index that is steeper than average (-1.9). This spectral index is still compatible with our nondetection, which constrains the spectral index to values > -2.3 .

For J1907+0602, very faint radio emission has been reported at 1510 MHz (Abdo et al. 2010; Ray et al. 2011). This is consistent with our nondetection and constrains the spectral index to values > -3.1 .

Finally, for J2032+4127, faint radio emission has been reported at 2000 MHz (Camilo et al. 2009; Ray et al. 2011). Extrapolating their flux measurement to our observing frequency with an assumed spectral index of -1.6 gives a flux value 20% higher than the upper limit derived from our observations. Considering typical errors on flux density measurements and the variability of pulsars, our nondetection is compatible with the detection at 2000 MHz. It can also be explained by either variations in the pulsar's emission (either intrinsic or due to scintillation on a timescale larger than the duration of the observation), or a spectral break or turnover in the 100–200 MHz range. Alternatively, it could be undetectable because of a flatter spectral index than the average. Indeed, for a spectral index shallower than -1.5 , which is compatible with the range of spectral indices discussed above, the extrapolated flux is compatible with our nondetection.

In all cases, our observations provide the most constraining upper limits at 150 MHz for the set of 27 pulsars we observed. Based on the comparison above, J0631+0636 and J2032+4127 would be the most interesting targets for potential reobservations at 150 MHz.

5. Beaming, revisited

5.1. Simple expectations

In Sect. 2.2, for simple RFM, we have provided a beam width of $\rho_{1400} = 16.8^\circ$ at 1400 MHz, and $\rho_{150} = 22.5^\circ$ for the HBA

⁵ <https://github.com/2ba0rNot2ba/mscorpol>

⁶ For detected pulsars, we want to compare the upper limits to measured values. For this reason, we used the nominal flux density values, assuming $W/P = 0.1$, rather than the measured flux density (with the measured value for the fractional pulse width W/P), see Appendix A.

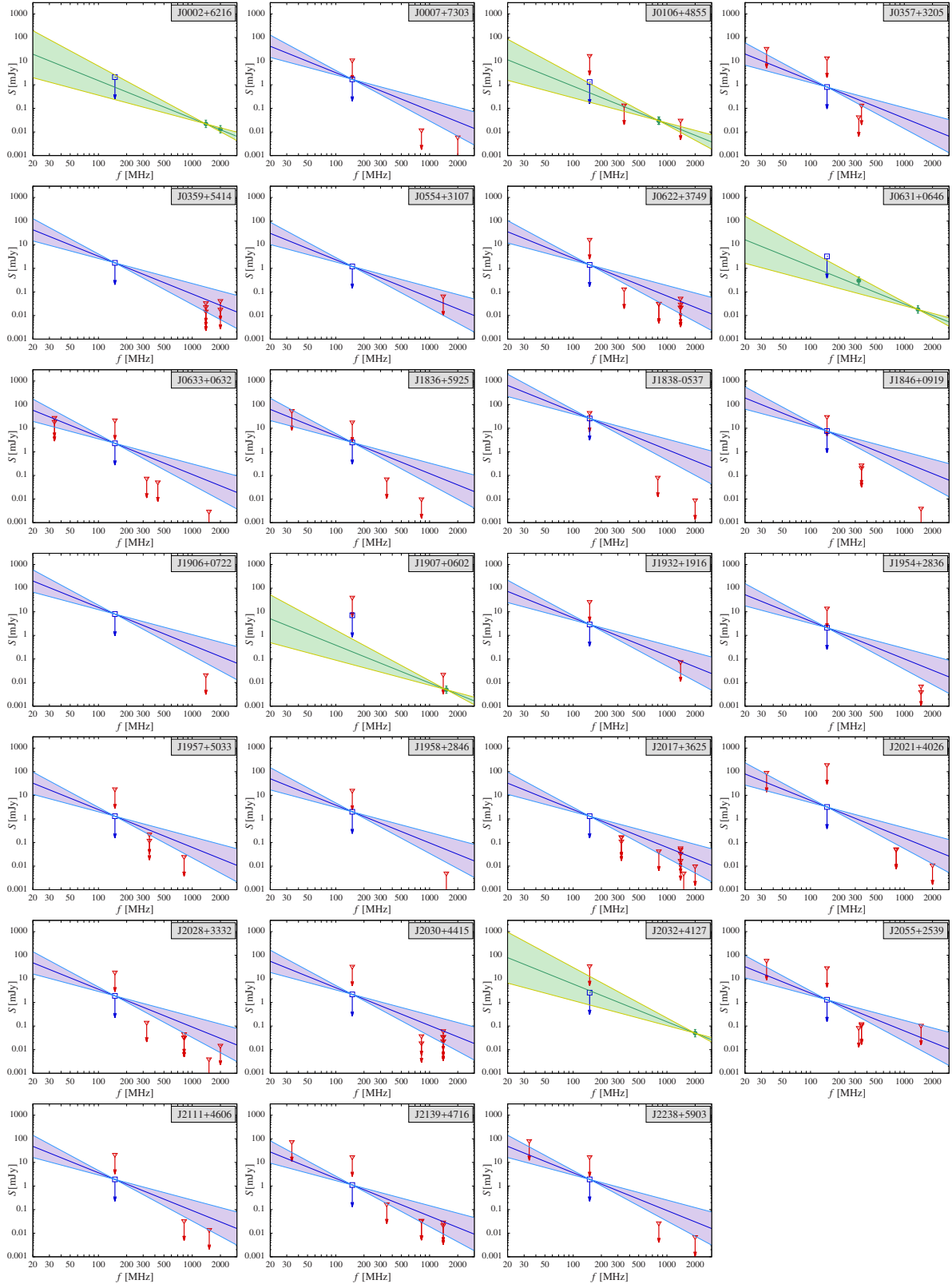


Fig. 1. Flux density upper limits for 27 radio-quiet gamma-ray pulsars, based on observations with LOFAR/FR606. Empty red triangles (with arrows): Flux density limits from previous observations. Filled green circles: Flux density measurements from previous observations (a typical error bar of 30% is indicated). Empty blue squares (with arrows): Flux density limits from this study. Dark blue line: Equivalent flux density limits for our observation (assuming a spectral index of -1.6). Shaded area between the light blue lines: Equivalent flux density limits for our observation for a spectral index of -1.6 ± 0.54 . Dark green line: Same as the dark blue line, but with respect to the most constraining detection. Shaded area between the light green lines: Same as the shaded area between the light blue lines, but with respect to the most constraining detection.

range (150 MHz). The angle ζ can have values in the range from $0^\circ \leq \zeta \leq 90^\circ$.

For any given value of α , the pulsar is geometrically visible (potentially RL) if the line of sight is not too far from the magnetic axis, $(\alpha - \rho) < \zeta < (\alpha + \rho)$. Uncertainties in α and ζ ($\Delta\alpha$ and $\Delta\zeta$) are accounted for, such that the pulsar is only classified as RL if this condition is satisfied for all values of $\alpha \pm \Delta\alpha$ and $\zeta \pm \Delta\zeta$. If $\zeta < \alpha - \rho$ or $\alpha + \rho < \zeta$ (again, accounting for the uncertainties in α and ζ), the pulsar is considered as RQ. In all other cases (the pulsar could be either RL or RQ depending on the precise values of α and ζ within the uncertainties), the pulsar is considered RF.

Figure 2 shows the (α, ζ) plane. The values shown for the pulsars are explained in the next section. A few of these pulsars should be geometrically visible. This is expected, for example, for the pulsar with $(\alpha = 85^\circ, \zeta = 84^\circ)$ in Fig. 2b. As the beam is wider at a low frequency ($\rho_{150} > \rho_{1400}$), a pulsar can be RQ at 1400 MHz, but RL at 150 MHz. If we assume a fully uniform distribution of α and ζ and no uncertainties ($\Delta\alpha = \Delta\zeta = 0$), approximately 20% of the pulsars that are RQ at 1400 MHz could be RL at 150 MHz. For our sample of 27 pulsars, this could mean on the order of five detections at 150 MHz with FR606.

Of course, a uniform distribution of α and ζ is not expected, and the uncertainties of α and ζ have to be taken into account. In the following, we estimate the values of α and ζ for the 27 pulsars of our sample, based on their gamma-ray profiles, and we attempt to improve our estimate of how many pulsars may have been detectable.

5.2. Pulsar geometry from gamma-ray profiles

Gamma-ray beams are very narrow in neutron star longitude due to concentration of the gamma-radiating electrons and positrons along “caustically” focused magnetic field lines; however, they are very broad in latitude, being brightest near the neutron star equator, and fading toward the poles. Beam shapes depend on several parameters: The open field line configuration varies with α and r_{LC} , and electron acceleration gap sizes depend on magnetic field strength. Gamma-ray emission models (see below) differ in how they exploit these parameters, but all have in common that “in fine” an observed profile depends on α and ζ . In the following we use the observed gamma-ray profiles to constrain the pulsar geometry (in terms of α and ζ), and thus refine our prediction of how many, and which, of our pulsars may be radio-detectable at low frequency.

We first made weighted gamma-ray pulse profiles for our sample, integrated above 100 MeV. Phases were calculated using tempo2 and rotation ephemerides were derived from LAT data for use in 3PC using the methods of Kerr et al. (2015). Weights, that is the probability that a given photon comes from the pulsar and not from a background source, were calculated using the methods of Kerr (2011). In all cases, the lightcurves were compatible with those previously published, such as in 2PC.

The weight calculation requires a spectral and spatial analysis of the region surrounding the pulsar. For our analysis, we used the results of the FL8Y source list⁷ applied to Pass 8 (P8R2) LAT data corresponding to events within 3° of each pulsar spanning 2008-08-04 to 2016-08-04. Our timing solution for J1932+1916 folds poorly beyond 2013-07-04 and so we used just under 5 years of data for that pulsar. Our LAT data sets include events belonging to the SOURCE class as defined

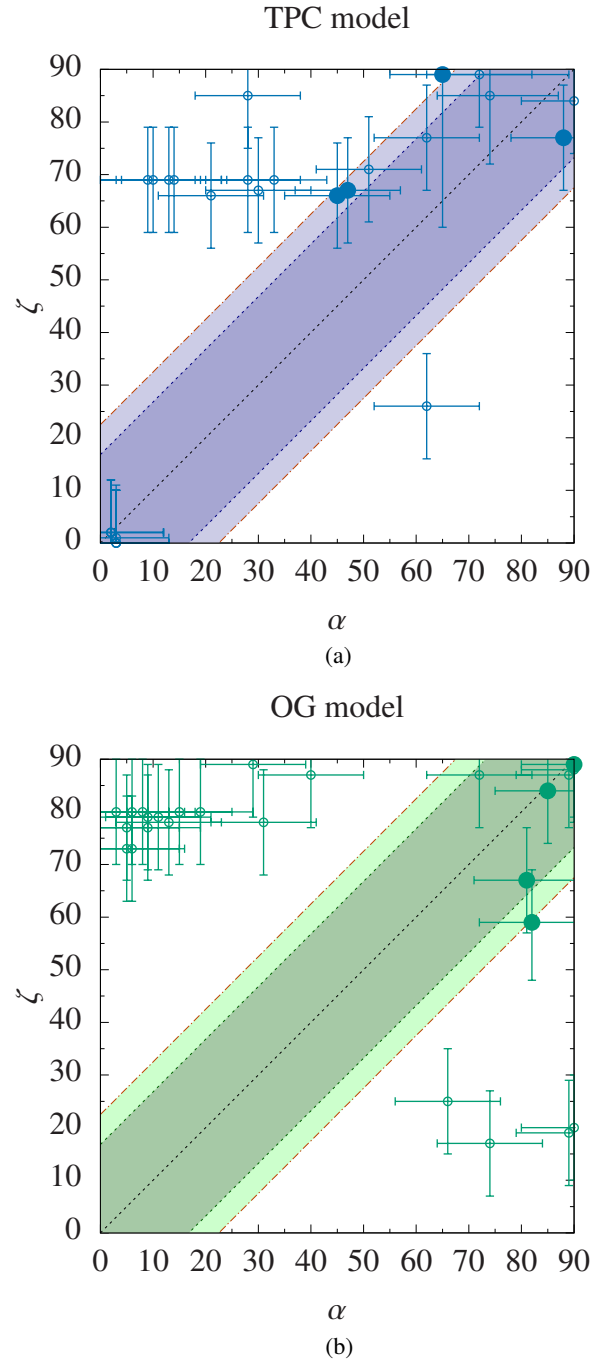


Fig. 2. Pulsar viewing geometry, expressed by the angles α and ζ , obtained by a fit to the gamma-ray data with the TPC model (panel a) and with the OG model (panel b). Pulsars on the dashed diagonal line ($\alpha = \zeta$) beam their radio emission to Earth regardless of their beam opening angle. Radio emission from pulsars between the two colored dashed lines is only detectable if their respective beam width $\rho \leq 16.8^\circ$, whereas pulsars between the two dash-dotted lines are visible if $\rho \leq 22.5^\circ$. Pulsars detected in radio are shown with large filled circles; pulsars without detected radio emission are shown with small empty circles.

⁷ See <https://fermi.gsfc.nasa.gov/ssc/data/access/lat/fl8y/>

⁸ See https://www.slac.stanford.edu/exp/glast/groups/canda/lat_Performance.htm

We then compared the gamma-ray profiles with the predictions from the outer gap (OG) model and the two-pole caustic (TPC) model, generated over a broad parameter space. Specifically, we used the same simulations and pulse-profile fitting techniques as Wu et al. (2018) (for more details on the simulation and fitting see Johnson et al. 2014). References to the OG and TPC models are given there. For J0002+6216, J0106+4855, J0631+0646, J1907+0602, and J2032+4127, we jointly fit the gamma-ray and radio profiles, using the 1400, 820, 1400, 1400, and 2000 MHz pulse profiles, respectively. As in Wu et al. (2018), we could not produce acceptable fits for J0631+0646. Compared to Wu et al. (2018), our analysis includes more gamma-ray photons, leading to updated results, especially for J0002+6216 and J2017+3625.

Table 2 lists the resulting α and ζ angles, with Cols. 2 and 3 for the OG model, and Cols. 4 and 5 for the TPC model. These results are also shown in Fig. 2. Most of the fits are limited by systematic uncertainties of $\sim 10^\circ$ (see Johnson et al. 2014; Pierbattista et al. 2015, for more details).

From the best-fit geometries and using the radio cone model of Story et al. (2007), we predicted the radio detectability for each pulsar at 1400 MHz (Table 3, Cols. 2 and 4 for models TPC and OG) and 150 MHz (Table 3, Cols. 3 and 5 for models TPC and OG, respectively). RL means that our line of sight should intersect a bright part of the cone. RF suggests that our line of sight skims the cone edge, and RQ means that the cone completely misses Earth. Aligned and nearly aligned rotators are considered as RF.

The characteristic width of the simulated radio beam at 0.1% of the peak intensity is given by Eqs. (9) and (10) of Story et al. (2007). For our simulations, we used $P = 100$ ms and $\dot{P} = 1 \times 10^{-15} \text{ s s}^{-1}$, which gives a width of 16.8° at 1400 MHz and 22.5° at 150 MHz.

Column 6 in Table 3 reports $(-\ln(\text{likelihood}))_{\text{TPC}} - (-\ln(\text{likelihood}))_{\text{OG}}$. When this value is positive, the OG model describes the data better than the TPC model, and vice versa. Based on their experience fitting many pulsars, Johnson et al. (2014) found that an absolute value of ≥ 15 was needed in log likelihood difference to determine that one model was significantly favored over another. Based on this, the last column gives the preferred model for each pulsar (indicated in parentheses if the log likelihood difference is < 15). Similar to the conclusions drawn by Johnson et al. (2014), Pierbattista et al. (2015), and others, we did not find that one model predominantly describes gamma-ray pulse profiles better than another.

5.3. Geometry results and discussion

Table 2 shows our results for the geometric angles ζ and α for the models TPC and OG. The implications for (geometrical) detectability of radio emission at 150 MHz and 1400 MHz are shown in Table 3. The results are also shown in Fig. 2, where pulsars detected in radio are shown with large filled circles and pulsars without detected radio emission are shown with small empty circles.

In Table 3, pulsars with detected radio emission are denoted with a * in Col. 1. It can be seen that all of these are labeled as either RF or RL. Equivalently, all detected pulsars fall within or close to the shaded region in Fig. 2.

Only one of the pulsars labeled as RL at 1400 MHz (J2238+5903) has not been detected in radio. However, a non-detection does not rule out the presence of low-level radio emission.

Table 2. Pulsar geometry as derived from fitting the gamma-ray light curves.

Pulsar	α_{TPC} (deg)	ζ_{TPC} (deg)	α_{OG} (deg)	ζ_{OG} (deg)
J0002+6216*	47	67	81	67
J0007+7303	2	2	9	79
J0106+4855*	65^{+24}_{-10}	89^{+10}_{-29}	90	89
J0357+3205	3	0	3	80
J0359+5414	3	0	89	19
J0554+3107	3	1	9	77
J0622+3749	9	69	6	80
J0631+0646*	—	—	—	—
J0633+0632	74^{+13}_{-10}	85^{+10}_{-13}	90	88
J1836+5925	28	85	5	77
J1838–0537	10	69	13	78
J1846+0919	2	2	5	73
J1906+0722	30	67	74	17
J1907+0602*	45	66	82	59^{+10}_{-11}
J1932+1916	3	0	90	20
J1954+2836	62	77	8	80
J1957+5033	2	2	6	73
J1958+2846	33	69	31	78
J2017+3625	51	71	15	80
J2021+4026	62	26	29	89
J2028+3332	28	69	40	87
J2030+4415	72	89	72	87
J2032+4127*	88	77	85	84
J2055+2539	14	69	66	25
J2111+4606	13	69	11	79
J2139+4716	21	66	19	80
J2238+5903	90	84	89	87

Notes. Column 1: name of the pulsar (pulsars with known radio emission are denoted with *). Columns 2 and 3: best-fit values for the angles α and ζ for the TPC model. Columns 4 and 5: same as Cols. 2 and 3, but for the OG model. Unless otherwise stated, the error was considered to be ± 10 .

Considering the uncertainties of ζ and α , neither model has pulsars that are expected to be RQ at 1400 MHz, but RL at 150 MHz. This result is not surprising as the widening of the beam (from 16.8° to 22.5°) is smaller than the uncertainties of ζ and α ($\geq 10^\circ$), a pulsar can at most change from RQ (at 1400 MHz) to RF (at 150 MHz), or from RF to RL. This does indeed happen for two pulsars, using the respective preferred models, for which we thus expect a more favorable geometry at 150 MHz: J0633+0632 should be RL at 150 MHz, but RF at 1400 MHz, and thus it is a good candidate for reobservation at 150 MHz. The pulsar J2032+4127 (RL at 150 MHz, but RF at 1400 MHz) has been detected at 2000 MHz, and should geometrically be observable at 150 MHz. Our nondetection at 150 MHz gives useful constraints for the spectral index (Sect. 4). For this reason, this pulsar is another good candidate for reobservation at 150 MHz.

In Table 3, most pulsars are labeled as RQ and are thus not expected to be detectable in radio. Our nondetections are thus compatible with an unfavorable viewing geometry. In addition, we saw in Sect. 2.2 that RFM broadening is not observed for all pulsars, decreasing the number of expected detections. Finally, in Sect. 2.1 we have discussed why $S_{1400} \propto L_r/d^2$ might simply be below the FR606 HBA sensitivity, even if the beam sweeps Earth. Combining these factors, the

Table 3. Radio-loud and radio-quiet pulsars.

Pulsar	Flag _{TPC} ^{150 MHz}	Flag _{TPC} ^{1400 MHz}	Flag _{OG} ^{150 MHz}	Flag _{OG} ^{1400 MHz}	$\Delta(-\ln(\text{likelihood}))$ (TPC-OG)	Preferred model
J0002+6216*	RF	RF	RF	RF	54.3	OG
J0007+7303	RF	RF	RQ	RQ	548.1	OG
J0106+4855*	RF	RF	RL	RL	7.9	(OG)
J0357+3205	RF	RF	RQ	RQ	170.5	OG
J0359+5414	RF	RF	RQ	RQ	3.28	(OG)
J0554+3107	RF	RF	RQ	RQ	5.5368	(OG)
J0622+3749	RQ	RQ	RQ	RQ	-10.2	(TPC)
J0631+0646*	–	–	–	–	–	–
J0633+0632	RL	RF	RL	RL	-111.6	TPC
J1836+5925	RQ	RQ	RQ	RQ	-2889.0	TPC
J1838-0537	RQ	RQ	RQ	RQ	31.7	OG
J1846+0919	RF	RF	RQ	RQ	8.7	(OG)
J1906+0722	RQ	RQ	RQ	RQ	-22.0	TPC
J1907+0602*	RF	RF	RF	RF	316.5	OG
J1932+1916	RF	RF	RQ	RQ	19.1	OG
J1954+2836	RF	RF	RQ	RQ	-32.2	TPC
J1957+5033	RF	RF	RQ	RQ	35.5	OG
J1958+2846	RQ	RQ	RQ	RQ	336.1	OG
J2017+3625	RF	RF	RQ	RQ	-46.1	TPC
J2021+4026	RQ	RQ	RQ	RQ	-111.6	TPC
J2028+3332	RQ	RQ	RQ	RQ	235.9	OG
J2030+4415	RF	RF	RF	RF	-100.9	TPC
J2032+4127*	RL	RF	RL	RL	-470.6	TPC
J2055+2539	RQ	RQ	RQ	RQ	82.5	OG
J2111+4606	RQ	RQ	RQ	RQ	42.6	OG
J2139+4716	RQ	RQ	RQ	RQ	-19.8	TPC
J2238+5903	RL	RL	RL	RL	-295.8	TPC

Notes. Column 1: name of the pulsar (pulsars with know radio emission are denoted with *). Columns 2 and 3: prediction regarding observability of the pulsar at 150 and 400 MHz for the TPC model: RL = radio-loud, RF = radio-faint, RQ = radio-quiet. The flag is framed by a box if TPC is the preferred model for this pulsar (double box if the absolute value of Col. 6 is >15, see text for details). Columns 4 and 5: same as Cols. 2 and 3, but for the OG model. Column 6: difference in likelihood for TPC and OG model (see text for details). Column 7: preferred model (based on Col. 6). The model is indicated in parentheses if the absolute value of Col. 6 is <15.

nondetection of all 27 pulsars at 150 MHz is compatible with an average spectral index and with RFM-like beam-widening for most pulsars.

6. Conclusion

We have followed up on 27 radio-quiet gamma-ray pulsars at low radio frequencies (110–190 MHz). No pulsed radio emission was detected. We have established stringent upper limits on their low-frequency radio flux density, which are considerably

more constraining than previous limits in comparable frequency ranges.

Despite the beam-widening expected at low radio frequencies, the comparison to simulations shows that most of our non-detections can be explained by an unfavorable viewing geometry; for the remaining observations (especially those of pulsars detected at higher frequencies), the sensitivity of our setup was not sufficient.

Based on our geometrical simulations and flux density upper limits, our best candidates for follow-up observations at

150 MHz are J0633+0632 and J2032+4127. It should be noted that follow-up observations of pulsars detected in radio, even if only at a higher frequency, are easier to analyze as no search for the correct DM value is required. With this in mind, all five pulsars already detected in radio should be reobserved at 150 MHz, potentially except for J1907+0602 for which a low-frequency detection is only possible if the spectrum turns out to be exceptionally steep.

Observations at even lower frequencies (<100 MHz) could be performed with NenuFAR (Zarka et al. 2018, 2020; Bondonneau et al., in prep.). However, flux extrapolations will have to take the likely spectral turnover into account.

Acknowledgements. LOFAR, the Low-Frequency Array designed and constructed by ASTRON, has facilities in several countries, that are owned by various parties (each with their own funding sources), and that are collectively operated by the International LOFAR Telescope (ILT) foundation under a joint scientific policy. Nançay Radio Observatory is operated by Paris Observatory, associated with the French Centre National de la Recherche Scientifique and Université d'Orléans. We acknowledge the use of the Nançay Data Center computing facility (CDN – Centre de Données de Nançay). The CDN is hosted by the Station de Radioastronomie de Nançay in partnership with Observatoire de Paris, Université d'Orléans, OSUC and the CNRS. The CDN is supported by the Region Centre Val de Loire, département du Cher. The *Fermi* LAT Collaboration acknowledges generous ongoing support from a number of agencies and institutes that have supported both the development and the operation of the LAT as well as scientific data analysis. These include the National Aeronautics and Space Administration and the Department of Energy in the United States, the Commissariat à l'Energie Atomique and the Centre National de la Recherche Scientifique/Institut National de Physique Nucléaire et de Physique des Particules in France, the Agenzia Spaziale Italiana and the Istituto Nazionale di Fisica Nucleare in Italy, the Ministry of Education, Culture, Sports, Science and Technology (MEXT), High Energy Accelerator Research Organization (KEK) and Japan Aerospace Exploration Agency (JAXA) in Japan, and the K. A. Wallenberg Foundation, the Swedish Research Council and the Swedish National Space Board in Sweden. Additional support for science analysis during the operations phase is gratefully acknowledged from the Istituto Nazionale di Astrofisica in Italy and the Centre National d'Études Spatiales in France. This work performed in part under DOE Contract DE-AC02-76SF00515. Work at the Naval Research Laboratory is supported by NASA.

References

- Abdo, A. A., Ackermann, M., Ajello, M., et al. 2010, *ApJ*, **711**, 64
- Abdo, A. A., Ajello, M., Allafort, A., et al. 2013, *ApJS*, **208**, 17
- Bilous, A. V., Kondratiev, V. I., Kramer, M., et al. 2016, *A&A*, **591**, A134
- Bilous, A. V., Bondonneau, L., Kondratiev, V. I., et al. 2020, *A&A*, **635**, A75
- Bondonneau, L., Grießmeier, J. M., Theureau, G., & Serylak, M. 2017, in *Pulsar Astrophysics – The Next 50 Years*, eds. P. Weltevrede, B. Perera, L. L. Preston, & S. Sanidas, *IAU Symp.*, **337**, 313
- Bondonneau, L., Grießmeier, J.-M., Theureau, G., et al. 2020, *A&A*, **635**, A76
- Camilo, F., Ray, P. S., Ransom, S. M., et al. 2009, *ApJ*, **705**, 1
- Clark, C. J., Pletsch, H. J., Wu, J., et al. 2015, *ApJ*, **809**, L2
- Clark, C. J., Wu, J., Pletsch, H. J., et al. 2017, *ApJ*, **834**, 106
- Clark, C. J., Pletsch, H. J., Wu, J., et al. 2018, *Sci. Adv.*, **4**, eaao7228
- Cordes, J. M. 1978, *ApJ*, **222**, 1006
- Cordes, J. M., & Lazio, T. J. W. 2002, *ArXiv e-prints* [arXiv:astro-ph/0207156]
- Cordes, J. M., & McLaughlin, M. A. 2003, *ApJ*, **596**, 1142
- Donner, J. Y., Verbiest, J. P. W., Tiburzi, C., et al. 2019, *A&A*, **624**, A22
- Frail, D. A., Jagannathan, P., Mooley, K. P., & Intema, H. T. 2016, *ApJ*, **829**, 119
- Gil, J., Gupta, Y., Gothoskar, P. B., & Kijak, J. 2002, *ApJ*, **565**, 500
- Hamaker, J. P. 2006, *A&A*, **456**, 395
- Haslam, C. G. T., Salter, C. J., Stoffel, H., & Wilson, W. E. 1982, *A&AS*, **47**, 1
- Hermesen, W., Kuiper, L., Basu, R., et al. 2018, *MNRAS*, **480**, 3655
- Hobbs, G. B., Edwards, R. T., & Manchester, R. N. 2006, *MNRAS*, **369**, 655
- Izvekova, V. A., Kuzmin, A. D., Malofeev, V. M., & Shitov, Y. P. 1981, *Astrophys. Space Sci.*, **78**, 45
- Jankowski, F., van Straten, W., Keane, E. F., et al. 2018, *MNRAS*, **473**, 4436
- Johnson, T. J., Venter, C., Harding, A. K., et al. 2014, *ApJS*, **213**, 6
- Johnston, S., & Karastergiou, A. 2017, *MNRAS*, **467**, 3493
- Kerr, M. 2011, *ApJ*, **732**, 38
- Kerr, M., Ray, P. S., Johnston, S., Shannon, R. M., & Camilo, F. 2015, *ApJ*, **814**, 128
- Kijak, J., & Gil, J. 1997, *MNRAS*, **288**, 631
- Kijak, J., & Gil, J. 1998, *MNRAS*, **299**, 855
- Kijak, J., & Gil, J. 2003, *A&A*, **397**, 969
- Kondratiev, V. I., Verbiest, J. P. W., Hessels, J. W. T., et al. 2015, *A&A*, **585**, A128
- Kuzmin, A. D., Malofeev, V. M., Shitov, Y. P., et al. 1978, *MNRAS*, **185**, 441
- Lawson, K. D., Meyer, C. J., Osborne, J. L., & Parkinson, M. L. 1987, *MNRAS*, **225**, 307
- Lazarus, P., Karuppusamy, R., Graikou, E., et al. 2016, *MNRAS*, **458**, 868
- Lorimer, D., & Kramer, M. 2005, *Handbook of Pulsar Astronomy* (Cambridge: Cambridge University Press)
- Lorimer, D. E., Yates, J. A., Lyne, A. G., & Gould, D. M. 1995, *MNRAS*, **273**, 411
- Maan, Y. 2015, *ApJ*, **815**, 126
- Maan, Y., & Aswathappa, H. A. 2014, *MNRAS*, **445**, 3221
- Maron, O., Kijak, J., Kramer, M., & Wielebinski, R. 2000, *A&AS*, **147**, 195
- Mereghetti, S., Kuiper, L., Tiengo, A., et al. 2016, *ApJ*, **831**, 21
- Michilli, D., Hessels, J. W. T., Donner, J. Y., et al. 2018, *MNRAS*, **476**, 2704
- Pierbattista, M., Harding, A. K., Grenier, I. A., et al. 2015, *A&A*, **575**, A3
- Pilia, M., Hessels, J. W. T., Stappers, B. W., et al. 2016, *A&A*, **586**, A92
- Pletsch, H. J., Guillemot, L., Allen, B., et al. 2012a, *ApJ*, **755**, L20
- Pletsch, H. J., Guillemot, L., Allen, B., et al. 2012b, *ApJ*, **744**, 105
- Pletsch, H. J., Guillemot, L., Allen, B., et al. 2013, *ApJ*, **779**, L11
- Porayko, N. K., Noutsos, A., Tiburzi, C., et al. 2019, *MNRAS*, **483**, 4100
- Rajwade, K., Seymour, A., Lorimer, D. R., et al. 2016, *MNRAS*, **462**, 2518
- Ray, P. S., Kerr, M., Parent, D., et al. 2011, *ApJS*, **194**, 17
- Saz Parkinson, P. M., Dormody, M., Ziegler, M., et al. 2010, *ApJ*, **725**, 571
- Siebert, W. 1973, *A&A*, **28**, 237
- Siebert, W., Reinecke, R., & Wielebinski, R. 1975, *A&A*, **38**, 169
- Smith, D. A., Bruel, P., Cognard, I., et al. 2019, *ApJ*, **871**, 13
- Stappers, B. W., Hessels, J. W. T., Alexov, A., et al. 2011, *A&A*, **530**, A80
- Story, S. A., Gonthier, P. L., & Harding, A. K. 2007, *ApJ*, **671**, 713
- Thorsett, S. E. 1991, *ApJ*, **377**, 263
- Tiburzi, C., Verbiest, J. P. W., Shaifullah, G. M., et al. 2019, *MNRAS*, **487**, 394
- van Haarlem, M. P., Wise, M. W., Gunst, A. W., et al. 2013, *A&A*, **556**, A2
- van Straten, W., & Bailes, M. 2011, *PASA*, **28**, 1
- van Straten, W., Demorest, P., & Osłowski, S. 2012, *Astron. Res. Technol.*, **9**, 237
- Wijnholds, S. J., & van Cappellen, W. A. 2011, *Proc. IEEE*, **59**, 1981
- Wu, H. K. 2018, PhD Thesis, Rheinische Friedrich-Wilhelms-Universität Bonn, Germany
- Wu, J., Clark, C. J., Pletsch, H. J., et al. 2018, *ApJ*, **854**, 99
- Xilouris, K. M., Kramer, M., Jessner, A., Wielebinski, R., & Timofeev, M. 1996, *A&A*, **309**, 481
- Yao, J. M., Manchester, R. N., & Wang, N. 2017, *ApJ*, **835**, 29
- Zarka, P., Coffre, A., Denis, L., et al. 2018, *The low-frequency radio telescope NenuFAR, 2018 2nd URSI Atlantic Radio Science Meeting (AT-RASC)*, <https://www.doi.org/10.23919/URSI-AT-RASC.2018.8471648>
- Zarka, P., Denis, L., Tagger, M., et al. 2020, *The low-frequency radio telescope NenuFAR*, <https://tinyurl.com/ycocd51y>

Appendix A: List of radio observations

Table A.1 lists all previous radio observations for our 27 targets.

The (upper limit) spectra of Figure 1 are based on the data in this table, as are Cols. 6–9 in Table 1. For detected pulsars, Figure 1 and Table 1 both use the nominal values (assuming $W/P = 0.1$). Column 1: pulsar name. Column 2: observing frequency. Column 3: pulsar detected in observation? (“y” if detected, blank

otherwise). Column 4: mean flux density or upper limit. For uniformity, this is the equivalent flux density (assuming $W/P = 0.1$). When available, the measured flux density (with the measured values of P and W) is given in a footnote. Column 5: telescope name. Column 6: frequency bandwidth of the observation. Column 7: observing time t (for observations of this work, we give the effective observing time $t_{\text{obs}}^{\text{eff}}$ instead, see Eq. (5)). Column 8: minimum S/N assumed by the authors. Column 9: duty cycle (W/P) assumed by the authors. Column 10: references.

Table A.1. List of radio observations, sorted by pulsar name, observing frequency, and publication date.

pulsar	f [MHz]	detect?	S [mJy]	telescope	Δf [MHz]	t or $t_{\text{obs}}^{\text{eff}}$ [h]	S/N_{min}	W/P	reference
J0002+6216	2000	y	0.013 ⁸	GBT	700	0.47	5	0.1	Clark et al. (2017), Wu et al. (2018), J. Wu (personal communication)
	1400	y	0.022 ⁸	Effelsberg	240	2	5	0.1	Clark et al. (2017), Wu et al. (2018), Wu (2018)
	150		<2.1	LOFAR/FR606	78.125	6.5	5	0.1	this work
J0007+7303	2000		<0.006	GBT	700	2.78	5	0.1	Ray et al. (2011)
	820		<0.012	GBT	48	19.6	5	0.1	Ray et al. (2011) and references therein
	150		<11	GMRT	16.7	0.25	5 ¹	n/a ⁴	Frail et al. (2016)
	150		<1.7	LOFAR/FR606	78.125	5.4	5	0.1	this work
J0106+4855	1400		0.031	Effelsberg	140	0.75	5	0.1	Pletsch et al. (2012b)
	820	y	0.020 ⁷	GBT	200	0.75	5	0.1	Pletsch et al. (2012b)
	820	y	0.020 ⁷	GBT	200	0.75	5	0.1	Pletsch et al. (2012b)
	350		<0.136	GBT	100	0.53	5	0.1	Pletsch et al. (2012b)
	150		<17	GMRT	16.7	0.25	5 ¹	n/a ⁴	Frail et al. (2016)
	150		<1.3	LOFAR/FR606	78.125	10.4	5	0.1	this work
J0357+3205	350		<0.134	GBT	100	0.5	5	0.1	Ray et al. (2011)
	327		<0.043	Arecibo	50	2	5	0.1	Ray et al. (2011)
	150		<13.5	GMRT	16.7	0.25	5 ¹	n/a ⁴	Frail et al. (2016)
	150		<0.8	LOFAR/FR606	78.125	8.9	5	0.1	this work
	34		<34	Gauribidanur	1.53	12	5	0.1	Maan & Aswathappa (2014) ²
J0359+5414	2000		<0.018	GBT	700	0.67	5	0.1	Clark et al. (2017), Wu et al. (2018)
	2000		<0.042	GBT	700	0.12	5	0.1	Clark et al. (2017), Wu et al. (2018)
	1400		<0.034	Effelsberg	240	0.53	5	0.1	Clark et al. (2017), Wu et al. (2018)
	1400		<0.023	Effelsberg	240	1	5	0.1	Clark et al. (2017), Wu et al. (2018)
	1400		<0.015	Effelsberg	240	1.92	5	0.1	Clark et al. (2017), Wu et al. (2018)
	150		<1.7	LOFAR/FR606	78.125	10.5	5	0.1	this work
J0554+3107	1400		<0.066	Effelsberg	260	1	5	0.1	Pletsch et al. (2013)
	150		<1.2	LOFAR/FR606	78.125	7.6	5	0.1	this work
J0622+3749	1400		<0.030	Effelsberg	250	0.53	5	0.1	Pletsch et al. (2012b)
	1400		<0.053	Effelsberg	250	0.17	5	0.1	Pletsch et al. (2012b)
	1400		<0.022	Effelsberg	250	0.87	5	0.1	Pletsch et al. (2012b)
	1400		<0.022	Effelsberg	250	0.92	5	0.1	Pletsch et al. (2012b)
	820		<0.032	GBT	200	0.75	5	0.1	Pletsch et al. (2012b)
	820		<0.032	GBT	200	0.75	5	0.1	Pletsch et al. (2012b)
	350		<0.131	GBT	100	0.53	5	0.1	Pletsch et al. (2012b)
	150		<16.5	GMRT	16.7	0.25	5 ¹	n/a ⁴	Frail et al. (2016)
	150		<1.4	LOFAR/FR606	78.125	5.6	5	0.1	this work

Notes. ¹: flux density upper limit calculated as 5 times the 1σ image noise given by Frail et al. (2016), their Table 3. ²: their periodic search. ³: this paper combines new data with previous data from Maan & Aswathappa (2014) ⁴: the upper limit resulting from their imaging data represents an averaged flux density (averaged over 16.1 s). ⁵: nominal flux density limit $S = 0.005$ mJy (assuming $W/P = 0.1$); detected flux density $S = 0.0034$ mJy (with $W/P \sim 0.03$). ⁶: nominal flux density limit $S = 0.050$ mJy (assuming $W/P = 0.1$); detected flux density $S = 0.120$ mJy. ⁷: nominal flux density limit $S = 0.030$ mJy (assuming $W/P = 0.1$); detected flux density $S = 0.020$ mJy (with $W/P \sim 0.02$). ⁸: nominal flux density limit.

Table A.1. continued.

pulsar	f [MHz]	detect?	S [mJy]	telescope	Δf [MHz]	t or $t_{\text{obs}}^{\text{eff}}$ [h]	S/N_{min}	W/P	reference
J0631+0646	1510	y	–	Arecibo	300	1.15	5	0.1	Clark et al. (2017), Wu et al. (2018)
	1400	y	0.018 ⁸	Effelsberg	240	2	5	0.1	Clark et al. (2017), Wu et al. (2018), J. Wu (personal communication)
	327	y	0.3 ⁸	Arecibo	68	1.25	5	0.1	Clark et al. (2017), Wu et al. (2018), J. Wu (personal communication)
	150		<3.2	LOFAR/FR606	78.125	2.0	5	0.1	this work
J0633+0632	1510		<0.003	Arecibo	300	1.17	5	0.1	Ray et al. (2011)
	430		<0.052	Arecibo	40	1.17	5	0.1	Ray et al. (2011)
	327		<0.075	Arecibo	50	0.83	5	0.1	Ray et al. (2011)
	150		<22	GMRT	16.7	0.25	5 ¹	n/a ⁴	Frail et al. (2016)
	150		<2.3	LOFAR/FR606	78.125	2.0	5	0.1	this work
	34		<28	Gauribidanur	1.53	22.5	5	0.1	Maan & Aswathappa (2014) ²
	34		<19	Gauribidanur	1.53	49.5	5	0.1	Maan (2015) ³
J1836+5925	820		<0.010	GBT	48	24	5	0.1	Ray et al. (2011)
	350		<0.070	GBT	100	2	5	0.1	Ray et al. (2011)
	150		<18	GMRT	16.7	0.25	5 ¹	n/a ⁴	Frail et al. (2016)
	150		<2.5	LOFAR/FR606	78.125	2.1	5	0.1	this work
	34		<55	Gauribidanur	1.53	16.5	5	0.1	Maan & Aswathappa (2014) ²
J1838–0537	2000		<0.009	A	B	C	D	E	Pletsch et al. (2012a)
	800		<0.082	A	B	C	D	E	Pletsch et al. (2012a)
	150		<45.5	GMRT	16.7	0.25	5 ¹	n/a ⁴	Frail et al. (2016)
	150		<26	LOFAR/FR606	78.125	0.6	5	0.1	this work
	1510		<0.004	Arecibo	300	1	5	0.1	Saz Parkinson et al. (2010)
J1846+0919	350		<0.272	GBT	100	0.5	5	0.1	Saz Parkinson et al. (2010)
	350		<0.209	GBT	100	0.85	5	0.1	Saz Parkinson et al. (2010)
	150		<30.5	GMRT	16.7	0.25	5 ¹	n/a ⁴	Frail et al. (2016)
	150		<7.6	LOFAR/FR606	78.125	0.9	5	0.1	this work
J1906+0722	1400		<0.021	Effelsberg	150	2	5	0.1	Clark et al. (2015)
	150		<8.0	LOFAR/FR606	78.125	3.0	5	0.1	this work
J1907+0602	1510	y	0.005 ⁵	Arecibo	300	0.92	5	0.1	Abdo et al. (2010), Ray et al. (2011)
	1400		<0.022	Arecibo	100	0.5	5	0.1	Ray et al. (2011)
	150		<40.5	GMRT	16.7	0.25	5 ¹	n/a ⁴	Frail et al. (2016)
	150		<7.1	LOFAR/FR606	78.125	3.2	5	0.1	this work
J1932+1916	1400		<0.075	Effelsberg	260	1	5	0.1	Pletsch et al. (2013)
	150		<26.5	GMRT	16.7	0.25	5 ¹	n/a ⁴	Frail et al. (2016)
	150		<2.9	LOFAR/FR606	78.125	4.1	5	0.1	this work
J1954+2836	1510		<0.007	Arecibo	300	0.33	5	0.1	Saz Parkinson et al. (2010)
	1510		<0.004	Arecibo	300	0.75	5	0.1	Saz Parkinson et al. (2010)
	150		<14	GMRT	16.7	0.25	5 ¹	n/a ⁴	Frail et al. (2016)
	150		<2.1	LOFAR/FR606	78.125	8.2	5	0.1	this work
J1957+5033	820		<0.025	GBT	200	1.36	5	0.1	Saz Parkinson et al. (2010)
	350		<0.225	GBT	100	0.25	5	0.1	Saz Parkinson et al. (2010)
	350		<0.122	GBT	100	0.85	5	0.1	Saz Parkinson et al. (2010)
	150		<18.5	GMRT	16.7	0.25	5 ¹	n/a ⁴	Frail et al. (2016)
	150		<1.3	LOFAR/FR606	78.125	8.6	5	0.1	this work
J1958+2846	1510		<0.005	Arecibo	300	0.67	5	0.1	Ray et al. (2011)
	150		<16	GMRT	16.7	0.25	5 ¹	n/a ⁴	Frail et al. (2016)
	150		<2.0	LOFAR/FR606	78.125	8.3	5	0.1	this work
J2017+3625	2000		<0.01	GBT	700	1	5	0.1	Clark et al. (2017), Wu et al. (2018)
	1510		<0.005	Arecibo	300	0.55	5	0.1	Clark et al. (2017), Wu et al. (2018)
	1400		<0.034	Arecibo	100	0.33	5	0.1	Clark et al. (2017), Wu et al. (2018)
	1400		<0.017	Effelsberg	240	0.25	5	0.1	Clark et al. (2017), Wu et al. (2018)

Table A.1. continued.

pulsar	f [MHz]	detect?	S [mJy]	telescope	Δf [MHz]	t or $t_{\text{obs}}^{\text{eff}}$ [h]	S/N_{min}	W/P	reference
J2021+4026	1398		<0.050	Nancay	128	1.08	5	0.1	Clark et al. (2017), Wu et al. (2018)
	1398		<0.058	Nancay	128	0.87	5	0.1	Clark et al. (2017), Wu et al. (2018)
	820		<0.043	GBT	200	0.75	5	0.1	Clark et al. (2017), Wu et al. (2018)
	327		<0.17	Arecibo	68	0.25	5	0.1	Clark et al. (2017), Wu et al. (2018)
	327		<0.17	Arecibo	68	0.25	5	0.1	Clark et al. (2017), Wu et al. (2018)
	327		<0.113	Arecibo	68	0.47	5	0.1	Clark et al. (2017), Wu et al. (2018)
	150		<1.3	LOFAR/FR606	78.125	8.1	5	0.1	this work
	2000		<0.011	GBT	700	1	5	0.1	Ray et al. (2011)
	820		<0.051	GBT	48	4	5	0.1	Ray et al. (2011)
	820		<0.053	GBT	48	4	5	0.1	Ray et al. (2011)
J2028+3332	150		<195	GMRT	16.7	0.25	5 ¹	n/a ⁴	Frail et al. (2016)
	150		<3.2	LOFAR/FR606	78.125	10.3	5	0.1	this work
	34		<92	Gauribidanur	1.53	12	5	0.1	Maan & Aswathappa (2014) ²
	2000		<0.015	GBT	700	0.5	5	0.1	Pletsch et al. (2012b)
	1510		<0.004	Arecibo	300	0.75	5	0.1	Pletsch et al. (2012b)
	820		<0.046	GBT	200	1	5	0.1	Pletsch et al. (2012b)
	820		<0.033	GBT	200	0.75	5	0.1	Pletsch et al. (2012b)
	820		<0.033	GBT	200	0.75	5	0.1	Pletsch et al. (2012b)
	327		<0.142	Arecibo	25	0.42	5	0.1	Pletsch et al. (2012b)
	150		<19	GMRT	16.7	0.25	5 ¹	n/a ⁴	Frail et al. (2016)
J2030+4415	150		<1.9	LOFAR/FR606	78.125	5.2	5	0.1	this work
	1400		<0.062	Effelsberg	250	0.17	5	0.1	Pletsch et al. (2012b)
	1400		<0.035	Effelsberg	250	0.53	5	0.1	Pletsch et al. (2012b)
	1400		<0.023	Effelsberg	250	1	5	0.1	Pletsch et al. (2012b)
	1400		<0.023	Effelsberg	250	1	5	0.1	Pletsch et al. (2012b)
	1400		<0.035	Effelsberg	140	0.75	5	0.1	Pletsch et al. (2012b)
	820		<0.038	GBT	200	0.75	5	0.1	Pletsch et al. (2012b)
	820		<0.019	GBT	200	3.05	5	0.1	Pletsch et al. (2012b)
	150		<33.5	GMRT	16.7	0.25	5 ¹	n/a ⁴	Frail et al. (2016)
	150		<0.019	LOFAR/FR606	78.125	10.1	5	0.1	this work
J2032+4127	2000	y	0.050 ⁶	GBT	700	1	5	0.1	Camilo et al. (2009), Ray et al. (2011)
	150		<35	GMRT	16.7	0.25	5 ¹	n/a ⁴	Frail et al. (2016)
	150		<2.6	LOFAR/FR606	78.125	9.6	5	0.1	this work
J2055+2539	1510		<0.106	Arecibo	300	0.5	5	0.1	Saz Parkinson et al. (2010)
	350		<0.124	GBT	100	0.67	5	0.1	Saz Parkinson et al. (2010)
	350		<0.11	GBT	100	0.85	5	0.1	Saz Parkinson et al. (2010)
	327		<0.085	Arecibo	50	0.5	5	0.1	Saz Parkinson et al. (2010)
	150		<29	GMRT	16.7	0.25	5 ¹	n/a ⁴	Frail et al. (2016)
	150		<1.3	LOFAR/FR606	78.125	5.3	5	0.1	this work
	34		<60	Gauribidanur	1.53	11	5	0.1	Maan & Aswathappa (2014) ²
J2111+4606	1520		<0.014	Lovell	200	14×1	5	0.1	Pletsch et al. (2012b)
	820		<0.033	GBT	200	1	5	0.1	Pletsch et al. (2012b)
	150		<21.5	GMRT	16.7	0.25	5 ¹	n/a ⁴	Frail et al. (2016)
	150		<1.9	LOFAR/FR606	78.125	7.2	5	0.1	this work
J2139+4716	1400		<0.022	Effelsberg	250	1	5	0.1	Pletsch et al. (2012b)
	1400		<0.029	Effelsberg	250	0.53	5	0.1	Pletsch et al. (2012b)
	820		<0.034	GBT	200	0.75	5	0.1	Pletsch et al. (2012b)
	820		<0.034	GBT	200	0.75	5	0.1	Pletsch et al. (2012b)
	350		<0.171	GBT	100	0.53	5	0.1	Pletsch et al. (2012b)
	150		<17	GMRT	16.7	0.25	5 ¹	n/a ⁴	Frail et al. (2016)
	150		<1.1	LOFAR/FR606	78.125	9.9	5	0.1	this work
	34		<74	Gauribidanur	1.53	11.5	5	0.1	Maan & Aswathappa (2014) ²
	2000		<0.007	GBT	700	2	5	0.1	Ray et al. (2011)
J2238+5903	820		<0.027	GBT	200	1.24	5	0.1	Ray et al. (2011)
	150		<17	GMRT	16.7	0.25	5 ¹	n/a ⁴	Frail et al. (2016)
	150		<1.9	LOFAR/FR606	78.125	9.7	5	0.1	this work
	34		<82	Gauribidanur	1.53	11	5	E	Maan & Aswathappa (2014) ²